

ABSTRACT

Title of Thesis: First Principles Computation Study and Design of δ -Bi₂O₃ Oxygen Ionic Conductors

Jonathon MacBride, Masters of Science, 2016

Thesis Directed By: Assistant Professor Yifei Mo,
Department of Material Science

The high operating temperatures in solid oxide fuel cells (SOFC) result in high cost, reduced longevity, and decreased efficiency impeding the wide application of this technology. Lowering the temperature of SOFC requires electrolytes with high ionic conductivity at lower temperatures. Stabilized δ -Bi₂O₃ electrolytes have high oxygen ionic conductivity, but its activation energy of ionic conduction increases below $\sim 600^\circ\text{C}$ due to the anion lattice ordering. We performed first principles computation to study this order-disorder transition in various dopant stabilized δ -Bi₂O₃ electrolytes. Using first principles computation, we predicted alternative dopants to lower the transition temperature of this material for future applications in SOFCs.

First Principles Computation Study and Design of δ -Bi₂O₃ Oxygen Ionic Conductors

by

Jonathon Kaine MacBride

Thesis submitted to the Faculty of the Graduate School of the
University of Maryland, College Park, in partial fulfillment
of the requirements for the degree of
[Masters of Science]
[2016]

Advisory Committee:
Professor Yifei Mo, Chair
Professor Eric Wachsman
Professor Chunsheng Wang

© Copyright by
[Jonathon Kaine MacBride]
[2016]

Acknowledgements

I would like to thank my advisor, Dr. Yifei Mo, without whom none of this would be possible. He patiently guided me in both my research and my writing. He provided me the tools with which to produce this work and feedback I needed to refine it.

I would like to thank committee members, Dr. Eric Wachsman and Dr. Chunsheng Wang, whose expert knowledge and experience were indispensable for the validation process.

I would like to acknowledge fellow graduate students Xingfeng He and Yizhou Zhu who have regularly provided technical guidance.

I would like to thank my employer, Specialty Granules Inc., and my boss, Dr. Rardon for the support and time needed to pursue this degree. They have consistently prioritized my individual development through this program and purposeful management.

Finally, I would like to thank my parents, sister, and wife. They provided encouragement, emotional support, and guidance. Without knowing they were behind me, I doubt I could have made it through this.

Author

Jonathon MacBride

Table of Contents

Acknowledgements.....	ii
Table of Contents	iii
List of Figures	iv
Chapter 1 : Introduction	1
1.1 Introduction to Solid Oxide Fuel Cells	1
1.2 δ -Bi ₂ O ₃ oxygen conductor as electrolyte for SOFC	4
1.3 Single Dopant Stabilized Bi ₂ O ₃	5
1.4 Double Doped Bi ₂ O ₃	7
Chapter 2 : Computational Method.....	11
2.1 Density Functional Theory Computation Method	11
2.2 Ewald Energy	12
2.3 Energy above Hull	12
2.4 Structures with Different Ordering	13
2.5 Transition Temperature.....	14
Chapter 3 : Oxygen Anion Sublattice in Pure Bismuth Oxide	16
3.1 Background	16
3.2 DFT calculation of Oxygen ordering in pure δ -Bi ₂ O ₃	18
Chapter 4 : Effect of Single Dopant Percentage and Ionic Radius	21
4.1 Lattice Constants.....	21
4.2 Effect of Er ³⁺ concentration on Transition Temperature	22
4.3 Effect of Single Dopant Type on Transition Temperature	23
Chapter 5 : Oxygen Sublattice Ordering in Double Doped δ -Bi ₂ O ₃	25
5.1 Determining Tungsten Dopant Oxidation State.....	25
5.2 Determining Oxygen Ordering around Tungsten Dopant	26
5.3 Calculation of Order-Disorder Transition Temperature	28
Chapter 6 : Computation Prediction of New Dopants	30
6.1 Prediction of Alternative Double Doping.....	30
6.2 Prediction of New Dopant for Double Doping	32
Chapter 7 : Future Work and Conclusions.....	37
7.1 Computation Error	37
7.2 Additional Alternative Dopants	37
7.3 Estimating phase stability	38
7.4 Experimental Verification.....	38
7.5 Conclusion	38
Bibliography	41

List of Figures

Figure 1.1. Arrhenius plot of conductivity and temperature for known SOFC electrolytes. [3]	2
Figure 1.2. 2x2x2 supercell showing crystal structure of δ -Bi ₂ O ₃ with disorder anion lattice according to Gattow et. al. 1962 [7].....	4
Figure 1.3. Arrhenius plot of DyWSB electrolytes by Wachsman et al. [17]	8
Figure 1.4. Arrhenius plot of DyGdSB electrolytes from Jung et. al. [19].....	9
Figure 2.1. Bi-O-Er phase diagram indicating decomposition of 20ErSB (20% erbia doped δ -Bi ₂ O ₃); generated using Materials Project [30] [31].....	13
Figure 3.1. Crystal structure of undoped δ -Bi ₂ O ₃ Bi ³⁺ (purple) and O ²⁻ (red) in 2x2x2 supercells initial structures with a) $\langle 1\ 1\ 1 \rangle$ vacancy ordering with variable coordination number; b) $\langle 1\ 1\ 1 \rangle$ vacancy ordering with constant coordination number; c) initial with $\langle 1\ 1\ 0 \rangle$ ordering; d) relaxed structure from b); e) relaxed $\langle 1\ 1\ 1 \rangle$ structure.	17
Figure 3.2. Energy above hull (E_{hull} , eV per atom) vs. initial Ewald energy (eV per atom) for 102 undoped δ -Bi ₂ O ₃ structures; includes both random anion orderings (blue) and two ordered states (red) shown in figure 3.1b and c.....	19
Figure 4.1. Graphs of M ³⁺ doped δ -Bi ₂ O ₃ lattice parameter vs M ³⁺ ionic radius or Er ³⁺ concentration: a) calculated lattice parameters, and b) experimental results by Jiang et al. [13].....	21
Figure 4.2. Calculated transition temperature (K) and E_{hull} energies (eV/atom) for 19-28% ErSB	23
Figure 4.3. Calculated transition temperature (K) and E_{hull} energies (eV/atom) for Yb ³⁺ , Er ³⁺ , Ho ³⁺ , Dy ³⁺ , and Sm ³⁺ in order of dopant ionic radius	24
Figure 5.1. Disordered and ordered energy above hull (eV/atom) for 12Dy6WSB for W ³⁺ , W ⁴⁺ , W ⁵⁺ , and W ⁶⁺	26
Figure 5.2. Ordered and disordered energy above hull for 6Dy3WSB based on different O ²⁻ occupancies at sites neighboring W ⁶⁺ cations.....	27
Figure 5.3. Calculated transition temperatures T_c (K) and energies above hull (E_{hull} , eV/atom) for DyW and DyGd doped systems	28
Figure 6.1. Calculated transition temperatures and energies above hull for 9 double doped electrolytes: 12 mol% (Dy, Er, Ho) 6 mol% (Gd, Sm, Nd)	31
Figure 6.2. E_{hull} energy from single calculation screening experiment for alternatives dopants to Gd ³⁺ in 12Dy6GdSB ordered left to right in order of substitution potential for Bi ³⁺ cations. Red line indicates E_{hull} for 12Dy6GdSB control.	32
Figure 6.3. E_{hull} energy from single calculation screening experiment for alternatives dopants to W ⁶⁺ in 12Dy6WSB ordered left to right in order of substitution potential for W ⁶⁺ cations. Red line indicates E_{hull} for 12Dy6WSB control.	33
Figure 6.4. Predicted transition temperatures and energies above hull for 12Dy6XSB (X is the proposed secondary dopant).....	34

Chapter 1 : Introduction

1.1 Introduction to Solid Oxide Fuel Cells

The combustion of hydrocarbon fuels is convenient but releases the greenhouse gas carbon dioxide. Carbon emissions can be reduced by utilization of renewable resources or significantly improving the efficiency of energy generation from combustible fuel sources in terms of energy produced per unit of fuel burned. Solid oxide fuel cells, SOFCs, are the most efficient means known to directly produce electrical energy from conventional fuels such as methane or gasified coal [1]. In SOFCs, an electrochemical reaction is mediated by oxygen conduction through a metal oxide based electrolyte. Ionic conductivity increases with temperature and decreases with thicknesses. Most proposed SOFCs require a high operating temperature (700-1000°C) [2] to reach a minimum operating conductivity for electrolyte thicknesses that can be economically mass produced. These high temperatures increase cost and reduce durability. Stabilized δ -phase bismuth oxides have the highest known oxygen conductivity for SOFC electrolytes but experience an increase in the activation energy below 600°C which reduces ionic conductivity. This change, usually noted as a bend in the Arrhenius plot, is due to a configurational transition from a disordered to an ordered O^{2-} anion lattice. Here, we utilize first principle calculations to search for a dopant strategy that can decrease this order-disorder transition temperature. [3]

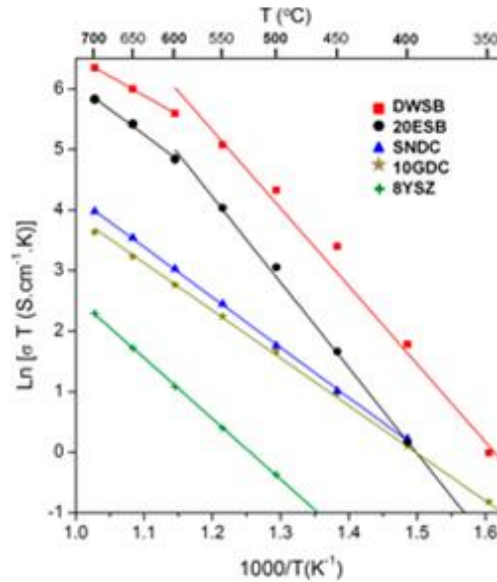


Figure 1.1. Arrhenius plot of conductivity and temperature for known SOFC electrolytes. [3]

Fuel cells in general have a high efficiency compared to traditional generators. Whether in coal fired power plants or cars, electricity production from hydrocarbon fuels requires a multistage process involving heat and mechanical energy. Every energy conversion is associated with some loss. The Carnot cycle, in particular, institutes a strict maximum efficiency for the generation of mechanical energy from heat. SOFCs directly convert chemical energy into electrical energy allowing much higher efficiencies.

Hydrogen fuel cells use individual protons as the charge carrier and the electromotive force (emf) is generated by the condensation reaction (reaction of oxygen and hydrogen to produce water). These fuel cells are efficient but require hydrogen or a fuel source which can be readily catalyzed into hydrogen at the anode. While hydrogen gas can be produced by electrolysis of water molecules or direct

hydrogen fermentation, it is more economical to produce it from reforming natural gas or gasification of coal or biomass [4]. SOFCs are capable of producing energy directly from these fuels such as CH_4 , or other gasification products, such as CO . This fuel flexibility allows more efficient use of the fuels within the current energy infrastructure.

SOFCs are primarily composed of four components: the anode, cathode, electrolyte, and interconnect. At the cathode, the fuel is oxidized providing the electromotive force. The oxygen for this reaction is absorbed at the anode forming O^{2-} ions and electrons. 2- charged oxygen ions are transported between the cathode and the anode through the electrolyte. As the electrolyte is not electrically conductive, the electrical current passes through the interconnect. The electrolytes must have high ionic conductivities to reduce Joule heating, low electronic conductivity to prevent leakage, and be impenetrable to gases.

The most widely used electrolyte for use in SOFCs is currently yttria-stabilized zirconia (YSZ) due to its high stability. Pure Zirconia (ZrO_2) has a high temperature cubic fluorite structure. Substituting between 4 and 8 mol % Y^{3+} in place of Zr^{4+} stabilizes this phase down to room temperature by increasing entropy of both cation and anion lattices, and significantly increases conductivity by adding stable vacant oxygen sites. As seen in figure 1, YSZ has a low conductivity compared to other potential SOFC electrolytes. This low ionic conductivity leads to a high operating temperature of at least $700\text{ }^\circ\text{C}$. [5] This increases operating costs, restricts material selection, and increases fatigue due to thermal cycling.

1.2 δ - Bi_2O_3 oxygen conductor as electrolyte for SOFC

δ - Bi_2O_3 has the highest oxygen ion conductivity reported for any SOFC electrolyte. This is largely due to the high ionic polarizability of bismuth, which increases oxygen mobility, and a defective fluorite structure [6] where 25% of the oxygen sites are unoccupied. Figure 1.2 shows a 2x2x2 supercell used to describe this high temperature δ -phase.

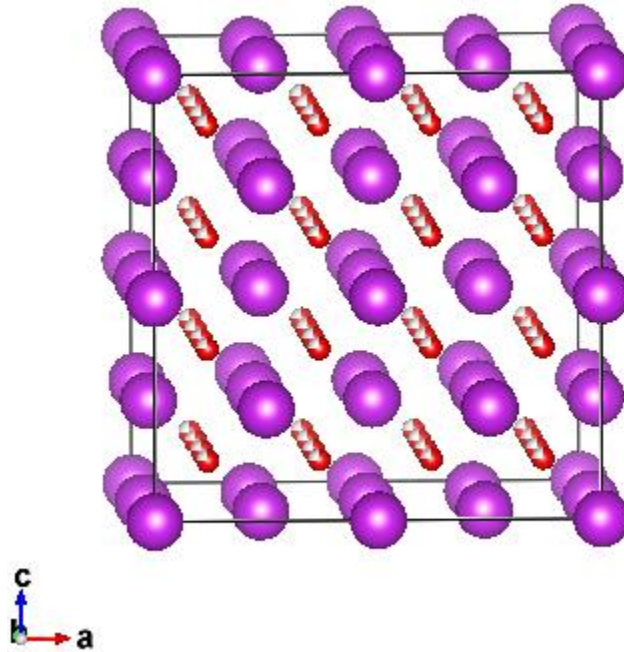


Figure 1.2. 2x2x2 supercell showing crystal structure of δ - Bi_2O_3 with disorder anion lattice according to Gattow et. al. 1962 [7].

δ - Bi_2O_3 is, however, a high temperature phase that is only stable between 730°C and its melting point 825°C. Below 730°C, the monoclinic α phase with a $P 1 2_{1/c} 1$ space group is more stable [8]. This α phase does not exhibit the same high number of oxygen vacancies and does not have a high conductivity as observed in the second order discontinuity in the Arrhenius plot. The δ phase has also been shown to transition into the β phase at 650°C or a bcc γ phase at 643°C. Both of these phases

are metastable. When $\delta\text{-Bi}_2\text{O}_3$ is stabilized at lower temperatures it may be used as an electrolyte for SOFCs.

1.3 Single Dopant Stabilized Bi_2O_3

Similar to the yttria in YSZ, several different single-dopants have been shown to stabilize $\delta\text{-Bi}_2\text{O}_3$ at lower temperatures. [9] From 1980 to 1983, Verkerk and Burggraaf published several papers evaluating $\delta\text{-Bi}_2\text{O}_3$ stabilized with single lanthanide dopants of the form M_2O_3 such as Dysprosium (Dy^{3+}) or Erbium (Er^{3+}). Ionic conductivity was shown to increase with a lower dopant concentration and with the larger ionic radii of the Ln^{3+} dopant. These trends can be attributed to reducing the disparity between the pure and doped $\delta\text{-Bi}_2\text{O}_3$ lattice parameters which decreases the activation energy.

Verkerk and Burggraaf [10] identified that 20 mol % erbia stabilized $\delta\text{-Bi}_2\text{O}_3$ (20ErSB) which has the highest ionic conductivity (37 S/m at 973K) observed without the addition of a second dopant. The cubic phase is stable from 17.5-45.5 mol % Er_2O_3 . Below that concentration, a mixture of multiple phases including α and β phases were observed. The high conductivity observed is attributed, in part, to this low dopant concentration at which other single dopants would not stabilize the cubic phase.

As the ionic radius increases above that of erbium, the minimum concentration to stabilize the cubic phase increases. Dysprosium (Dy^{3+}) doped Bi_2O_3 is stable between 28.5-40 mol %. The conductivity is 0.71 S/m and 14.4 S/m at 500 °C and 700°C, respectively. [11] The defective fluorite structure of gadolinium (Gd^{3+}) doped Bi_2O_3 is stable from 10-50 mol % at high temperatures but below 35% the

electrolyte has a rhombohedral structure at 600°C. The conductivity of the stabilized rhombohedral phase (4.5 S/m) has a higher conductivity than the stabilized cubic phase (2.4 S/m) at 600°C which due to the larger required dopant concentrations (10 and 35 mol % respectively). [12] Lanthanum (La^{3+}) and other larger dopants cannot stabilize the $\delta\text{-Bi}_2\text{O}_3$ phase at any concentration. Several non-lanthanide dopants have been identified that can help stabilize the face centered cubic (fcc) phase including Y_2O_3 , WO_3 , Nb_2O_5 , and BaO [12].

There are two primary types of conductivity degradation for stabilized $\delta\text{-Bi}_2\text{O}_3$ electrolytes when annealed at lower temperatures: rhombohedral phase transition and anion ordering. The cubic defective fluorite structure with several dopants may transition to the lower conductivity rhombohedral phase when annealed at 650°C. If quenched to 500°C, the cubic phase, and therefore, anion order-disorder transition, can be observed for several dopants. The phase of this quenched state can be characterized with X-ray Powder Diffraction (XRD). [13]

In contrast, aged samples that have undergone anion lattice ordering are indistinguishable via XRD. At high temperatures, the anion lattice is disordered resulting in high entropy and high ionic conductivity. All literature sources indicate an order-disorder transition temperature between 550 and 600°C. Transmission electron microscopy (TEM) results indicate that vacancies tend to order along $\langle 1,1,1 \rangle$ [14] though $\langle 1,1,0 \rangle$ pairing is likely to form as well [15]. In addition, neutron diffraction results demonstrate anion sites shifting from the ideal fluorite 8c sites to 32f interstitial sites. While literature results do not seem to indicate that the order-disorder transition temperature is dependent on the dopant polarizability or

dopant loading, these factors control the kinetics of the transition and relative difference in conductivity. Higher dopant polarizability, which is proportional to ionic radius, reduces the rate of aging due to anion lattice ordering. Higher concentrations of dopants, such as Er^{3+} from 15% to 40%, decreased the relative conductivity decay and the rate of aging, but this lowers the initial conductivity.

1.4 Double Doped Bi_2O_3

Oxygen ionic conductivity of a stabilized bismuth oxide electrolyte is increased as total dopant concentration is decreased. The minimum concentration to stabilize the fluorite structure varies with the dopant. Meng et al. observed in 1988 that the addition of a second dopant increases the cation lattice entropy permitting stabilization at lower total dopant concentrations. Because the fcc phase has a higher degree of symmetry than $\alpha\text{-Bi}_2\text{O}_3$ or rhombohedral phases, it is entropically stabilized. In particular, yttrium (Y^{3+}), molybdenum (Mo^{6+}), niobium (Nb^{3+}), and tungsten (W^{6+}) were identified as useful dopants to stabilize the cubic phase. Barium (Ba^{2+}), strontium (Sr^{2+}), lanthanum (La^{3+}), praseodymium (Pr), samarium (Sm^{3+}), and gadolinium (Gd^{3+}) were identified to stabilize the rhombohedral phase.

Wachsman et al. co-doped Bi_2O_3 with WO_3 and Dy_2O_3 ; two dopants with high polarizability that had already been demonstrated to stabilize the fluorite structure individually [16]. While Dy^{3+} requires 28.5-50 mol % and W^{6+} requires 25 mol% minimum dopant concentration, 8Dy4WSB (8% Dy_2O_3 - 4% WO_3 stabilized bismuth oxide) is stable. It has a high ionic conductivity of 0.43 S/cm compared to 20ESB 0.21 S/cm at 500°C.

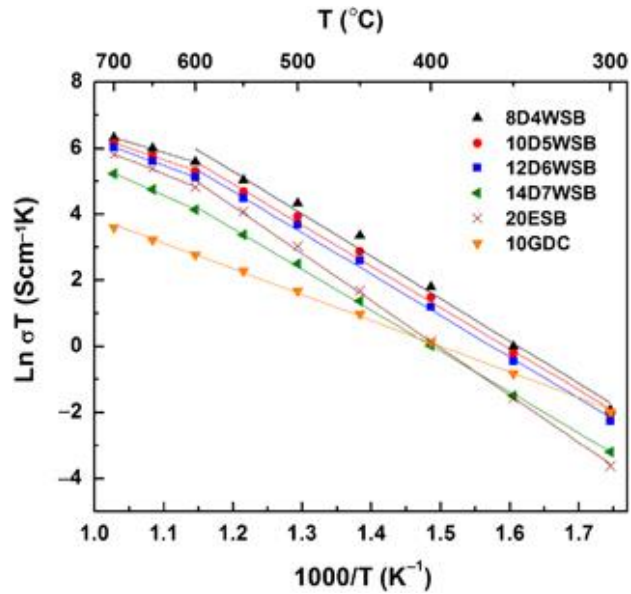


Figure 1.3. Arrhenius plot of DyWSB electrolytes by Wachsman et al. [17]

DyWSB electrolytes also exhibit aging due to phase change and anion ordering. The specific mechanism is dependent on the composition and temperature. 8Dy4WSB exhibits little aging when annealed at 600°C indicating that the order-disorder transition temperature is at or below this temperature. When annealed at 500°C, the conductivity loss is accompanied with the formation of an orthogonal phase as observed by XRD. Below 400°C, no orthogonal phase forms, and only aging due to order-disorder transition is observed, likely due to reduced kinetics at low temperature. Differential Thermal Analysis (DTA) results indicated that order-disorder transition still occurs at roughly the same temperature as single dopant system. For 12Dy6WSB and higher concentrations, little to no orthorhombic phase forms when annealed at 500°C. Both orthorhombic and tetragonal phases form when annealed at 600°C. The order-disorder transition temperature is likely to be 600°C.

Published Arrhenius plots of these systems, Figures 1.1 and 1.3, often show a curved line rather than the clear knee seen in single dopant plots. This is not observed for the higher concentrations of DyWSB in these figures but is seen for all concentrations [18]. This bend appears to occur below 600°C but that value is still used as the order disorder transition temperature for those systems in the literature.

Recently, a $\text{Bi}_2\text{O}_3\text{-Gd}_2\text{O}_3\text{-Dy}_2\text{O}_3$ system (dysprosium and gadolinium stabilized bismuth oxide) has been developed which was measured to have a comparable conductivity to DyWSB [19]. The optimum dopant concentration for this system is 8Dy4GSB (8% Dy_2O_3 , 4% Gd_2O_3 , 88% Bi_2O_3) which has a conductivity of 0.18 S/cm.

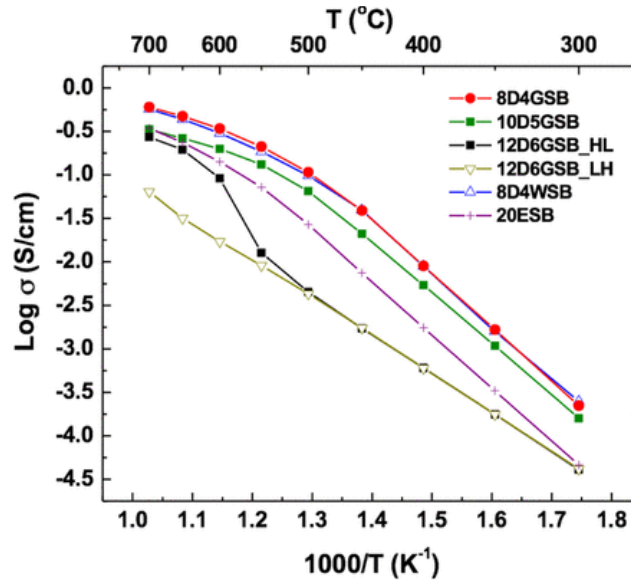


Figure 1.4. Arrhenius plot of DyGdSB electrolytes from Jung et. al. [19]

As previously noted, cubic Bi_2O_3 doped with dysprosium or gadolinium individually is stable at high concentrations but these larger dopants tend to favor the formation of a rhombohedral phase outside of a narrow solubility range. This double doped electrolyte frequently exhibits both cubic and rhombohedral phases. While

additional calcination produced a uniformly cubic phase, the amount of the rhombohedral phase increased as the total concentration or Gd:Dy ratio is increased. A multiphase phase composition occurs between 550 and 600°C for 12Dy6GdSB which seems to be unrelated to the order-disorder transformation. When held at 500°C, an aging behavior was observed for 8Dy4GdSB order-disorder transition observed. While the temperature was not reported by Jung et al, the Arrhenius plot seems to indicate that the transition occurs at roughly 525°C. Conductivity degradation was observed for 12Dy6GdSB and 10Dy5GdSB when annealed at 500°C. This trend seems to be driven by the cubic-rhombohedral transition instead of anion ordering. While this new phase has a lower conductivity than the fcc, it does not exhibit further conductivity degradation after it is formed. Therefore, this DyGdSB is a potential Bi₂O₃ based electrolyte with less order-disorder aging.

Chapter 2 : Computational Method

2.1 Density Functional Theory Computation Method

In this thesis, density function theory (DFT) calculations are performed to determine the energies and stabilities of ordered and disordered states of δ -Bi₂O₃ based electrolytes. The temperature for the transition between ordered and disordered states of oxygen sublattice is determined using thermodynamic calculations. In DFT, Hohenberg-Kohn theorems state that the ground-state electron density is uniquely determined by the external potential and that all other electron states within the same potential will have an equal or higher energy. DFT calculations approximate this ground state energy by solving the Kohn Sham equations. In this work, all DFT calculations were performed using VASP (Vienna Ab-initio Simulation Package) [20] [21] [22] [23]. The projector augmented wave approach (PAW) [24] [25], generalized gradient approximation (GGA) [26] [27], and gamma only method were used.

Initial ion placement and calculation parameters are stored in POSCAR, INCAR, POTCAR, and KPOINTS files. The POSCAR file contains all initial ion positions for an individual DFT calculation. Each initial supercell is cubic with 5.665 Å side length, contains 4 cation and 8 anion sites, and has a 75% oxygen site occupancy. The boundary conditions are periodic in all three directions. All structures are based on 2x2x2 supercells unless otherwise noted. Dopant percentages are restricted to 3.125% increments as the number of each ion type in a supercell must be an integer. For structure from literature such as 8Dy4WSB, ((DyO_{1.5})_{0.08}-(WO₃)_{0.04}-

($\text{BiO}_{1.5}$)_{0.88}), the integers represent the exact mol percentage of each dopant. In this thesis, all percentages are rounded to the nearest integer. 9Dy3WSB ($((\text{DyO}_{1.5})_{0.09375}(\text{WO}_3)_{0.03125}(\text{BiO}_{1.5})_{0.875})$) and 6Dy3WSB ($((\text{DyO}_{1.5})_{0.0625}(\text{WO}_3)_{0.03125}(\text{BiO}_{1.5})_{0.90625})$) are run on 2x2x4 supercells as they would contain 49.5 O²⁻ anions per 2x2x2 supercell.

The remaining files were generated using Pymatgen [28] in consistency with Material Project (materialsproject.org) [29] unless otherwise noted. This initiative started by Gerbrand Ceder and Kristin Persson from Lawrence Berkeley National Laboratory allows the results from our DFT calculations to be accurately compared to this databases existing material library. In order to ensure rapid convergence, Gaussian Smearing (ISMEAR = 0) was used and the number of K points was set to 1x1x1. During the relaxation of the supercell, the lattice parameter can either be fixed or allowed to relax (ISIF equals 2 or 3 respectively).

2.2 Ewald Energy

Before DFT is used to relax the supercell, the total electrostatic energy of the initial structure is calculated using the Ewald summation technique as incorporated into Pymatgen. One may screen initial structures with higher electrostatic energy prior to DFT calculations.

2.3 Energy above Hull

The energy of the relaxed system is generally reported in this thesis in terms of energy above hull (E_{hull} in eV/atom). This provides a reference frame to compare the relative stabilities of each structure and composition. For each material system,

Materials Project database was queried to generate a 0K isobaric phase diagram as shown in Figure 2.1. The smallest convex set of 1 to N stable phases describes the convex hull. The total energy (E_0 , eV/atom) output from VASP relaxation describes the internal energy of the system at 0K. The reported E_{hull} energy is the difference in this value and a stoichiometrically equivalent mixture of the phases in the convex hull normalized to the total number of ions. All E_{hull} values calculated in this thesis are positive.

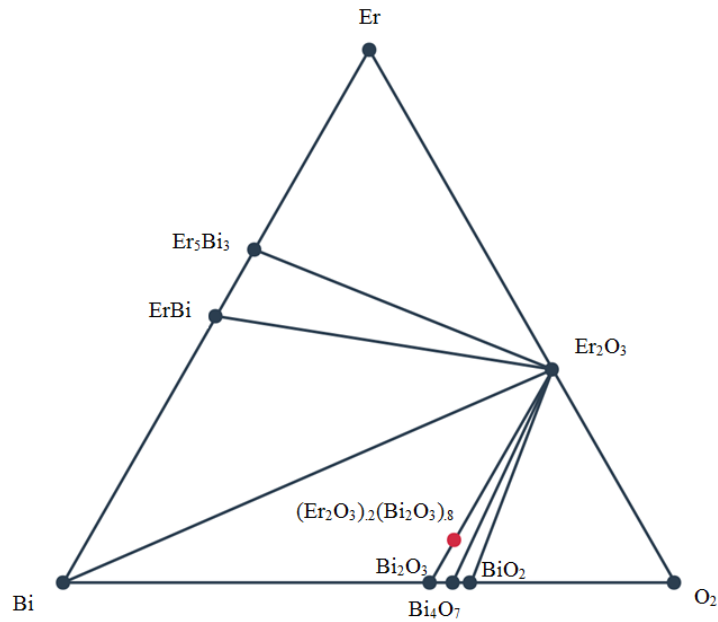


Figure 2.1. Bi-O-Er phase diagram indicating decomposition of 20ErSB (20% erbia doped δ -Bi₂O₃); generated using Materials Project [30] [31]

2.4 Structures with Different Ordering

The cations in stabilized δ -Bi₂O₃ diffuse at a much lower rate than the oxygen anions and can be considered immobile during the order-disorder transition. In this study, a fixed cation ordering is used, and fifty initial structures based on disordered anion and cation lattices were generated for each of the single and double doped

systems in chapters 4 and 5. If multiple calculations would have the same dopant charge and concentration (such as in section 4.3), the same initial ion positions are used. The cation ordering for the initial structure with the lowest final E_{hull} is used to generate initial configurations with fixed cation and disorder anions. The average E_{hull} for this series of orderings is used as the calculated energy for the disordered structure. The minimum E_{hull} observed during these simulations is used to represent the ordered structure.

2.5 Transition Temperature

The order-disorder transition temperature (T_c) describes the temperature at which the disordered state will transition into the ordered structure. As the systems are closed, isobaric, and isothermal, the thermodynamics are characterized by the Gibbs free energy,

$$G = H - TS = U + pV - TS \quad \text{(eq. 2.1.)}$$

where G is the Gibbs free energy, H is the enthalpy, S is the entropy, T is the temperature, E is the total internal energy, p is the external pressure, and V is the volume. The pV term is small for most solids and can be ignored. At T_c , the ordered and disordered states are in equilibrium and the Gibbs free energy for both states are equal.

The primary contribution to the change in entropy between the ordered and disordered states is the configurational entropy of the disordered anion lattice. Entropy associated with cation ordering or defects are excluded. The change in entropy (ΔS) per atom is calculated from Boltzmann's entropy formula as follows:

$$\Delta S = k_b \frac{1}{N} \ln \frac{(O_o + V_o)!}{O_o! V_o!} \quad (\text{eq. 2.2.})$$

$$\Delta S = \frac{-2k_b}{1 + 2x} (x \ln x + (1 - x) \ln(1 - x)) \quad (\text{eq. 2.3.})$$

where k_b is Boltzmann's constant, O_o is the number of oxygen ions, V_o is the number of oxygen vacancies, N is the total number of ions, and x is the occupancy of the oxygen sites. Equation 2.3 simplifies equation 2.2 by incorporating Stirling's approximation and cancelling out extrinsic variables such as N . For most of the calculations in this thesis with 3+ cations, x is equal to 0.75 and the entropy is 3.88×10^{-5} eV/K/atom. When dopants with different oxidation states, such as W^{6+} , are incorporated, oxygen lattice occupancy changes to ensure a neutral overall charge in the supercell.

DFT calculations provide the total internal energy (E) of the relaxed structure at 0K. E in the paper is reported in terms of E_{hull} (eV/atom) which provides a reference frame for comparison. As described in section 2.4, the energy of the disordered and ordered states are described by the average and minimum observed E_{hull} values for that particular system. With these assumptions, the Gibbs free energy (eq. 1.1) for the disordered and ordered states can be solved for the transition temperature as follows:

$$\Delta G = 0 = (E_{hd} - E_{ho}) - \Delta S T_c \quad (\text{eq. 2.4.})$$

$$T_c = \frac{E_{hd} - E_{ho}}{\Delta S} \quad (\text{eq. 2.5.})$$

where E_{hd} and E_{ho} are the E_{hull} energies for the disordered and ordered states, respectively, and ΔS is calculated from equation 2.3.

Chapter 3 : Oxygen Anion Sublattice in Pure Bismuth Oxide

3.1 Background

The physical properties of pure δ bismuth oxide are a direct result of its fluorite structure. Like all fluorite structures, the Bi^{3+} ions are situated in an fcc cation lattice and the O^{2-} ions are situated in a bcc anion lattice. As there are two O^{2-} sites for each Bi^{3+} site, the oxygen sublattice of Bi_2O_3 has 75% occupancy. The 25% unoccupied sites are often referred to as vacancies but are not defects in the crystal structure. The order-disorder transition occurs when these vacancies order into a low energy oxygen sublattice configuration referred to as the ordered state. This ordered sublattice has higher activation energy for ionic conduction than the disordered state resulting in lower conductivity at lower temperature. In 1938, L.G. Sillen described the structure of $\delta\text{-Bi}_2\text{O}_3$ with ordered sublattice with oxygen vacancies aligned along the $\langle 1\ 1\ 1 \rangle$ [32]. (Fig. 3.1a). Figure 3.1 a and b show two ordered sublattice as discussed by Wachsman *et al.* [33]. Figure 3.1a shows an oxygen sublattice configuration with the vacancies ordered along $\langle 1\ 1\ 1 \rangle$ in the 16f sites. The 8 vacancies in the supercell were arranged exclusively around two Bi^{3+} sites creating a large localized positive charge. For the other $\langle 1\ 1\ 1 \rangle$ vacancy ordered configuration in figure 3.1b, each Bi^{3+} site has exactly 2 neighboring vacancies.

Gattow and Schroeder's [7] description of the Bi^{3+} lattice agreed with the Sillen's work, but noted the discrepancy between the fixed anion positions and the experimentally observed high conductivity. In Gattow's description of the oxygen

sublattice configuration, shown in figure 1.2, the oxygen ions are located in the $8c$ sites with the vacancies evenly distributed. This structure of a disordered state is used to construct all of the initial structures for our calculations.

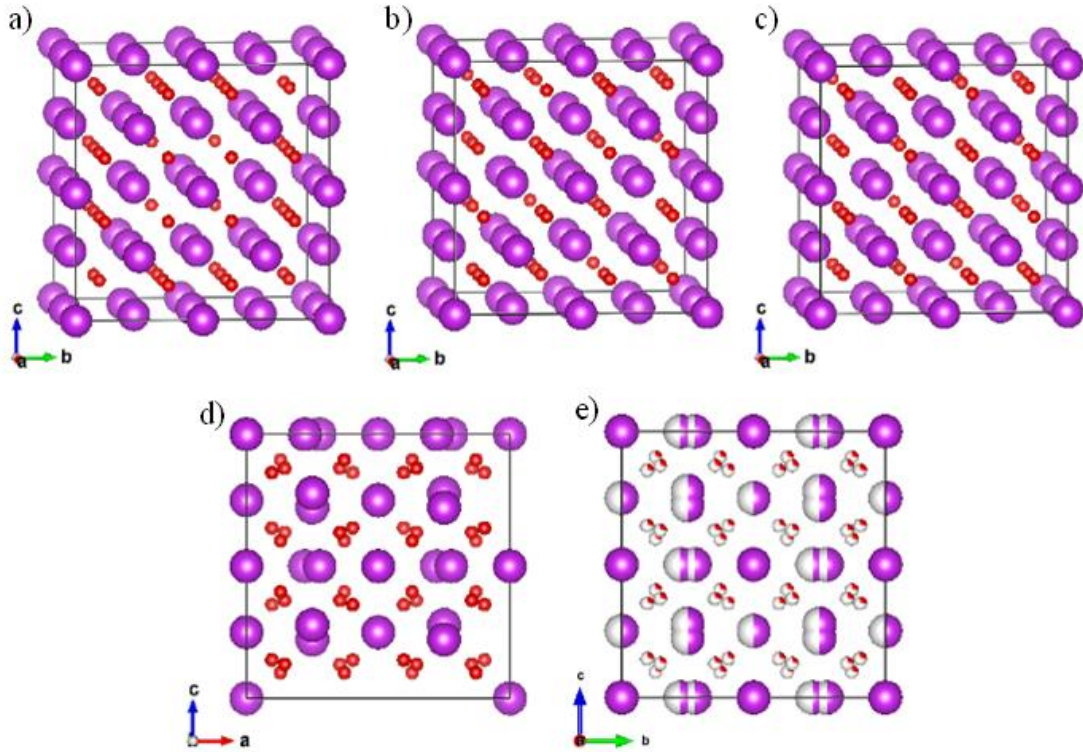


Figure 3.1. Crystal structure of undoped $\delta\text{-Bi}_2\text{O}_3$ Bi^{3+} (purple) and O^{2-} (red) in $2 \times 2 \times 2$ supercells initial structures with a) $\langle 1\ 1\ 1 \rangle$ vacancy ordering with variable coordination number; b) $\langle 1\ 1\ 1 \rangle$ vacancy ordering with constant coordination number; c) initial with $\langle 1\ 1\ 0 \rangle$ ordering; d) relaxed structure from b); e) relaxed $\langle 1\ 1\ 1 \rangle$ structure.

Further research indicates that the lattices are distorted from ideal fluorite structure used in Sillen and Gattow models. In 1963, Willis used neutron scattering of calcium fluoride (CaF_2) to show that the anions are not positioned in the ideal $8c$ sites.

Instead, each anion is displaced along a single tetragonal direction away from the nearest neighboring cation. As Bi_2O_3 should be similarly displaced, the disordered structure should have 32 oxygen sites (32f) at 3/16 occupancy. In 2009, Aidhy et al. performed first principles DFT calculations and determined the displacement of disordered oxygen ions positions in $\delta\text{-Bi}_2\text{O}_3$ [6] (Fig. 3.1e). Of the 4 Bi^{3+} sites in each unit cell, one site is displaced in each of the 3 cardinal directions and the remaining site is stationary. Each of the 8 disordered anion sites is replaced with three adjacent sites with 25% occupancy. In this study, we rely on the relaxation in the DFT calculations to capture these displacements. The equilibrium positions obtained from our calculations (Fig. 3.1d) are in good agreement with the previous results from literature (Fig. 3.1e).

3.2 DFT calculation of Oxygen ordering in pure $\delta\text{-Bi}_2\text{O}_3$

DFT calculations were performed to determine the structure and energies of Bi_2O_3 with ordered and disordered O sublattices. Using the methods described in Chapter 2, 100 distinctive structures with random anion orderings were generated and evaluated. The average energy of the 100 random oxygen sublattice orderings described the energy of the disordered state. In addition, the known ordered oxygen sublattices with two $\langle 1\ 1\ 1 \rangle$ and one $\langle 1\ 1\ 0 \rangle$ orderings [15] [33] (Figure 3.1 a, b, and c) were evaluated.

We compare the electrostatic Ewald energy with the actual DFT energy to understand the effects of electrostatics on the ordering of oxygen sublattice. The Ewald energies of the disorder sublattice vary between -27.3 and -28.6 with an average of -28.0 eV/atom, showing strong effect of electrostatic interactions among

ions on the energy of the sublattice. Similarly, the values of energy above hull (E_{hull}) from DFT calculations varied between 0.0550 and 0.103 with an average of 0.0736 eV/atom. The lowest energy structure of this series had an E_{hull} value of .0550 eV/atom and an Ewald energy of -28.38 eV/atom. There is a general correlation between Ewald and E_{hull} energy.

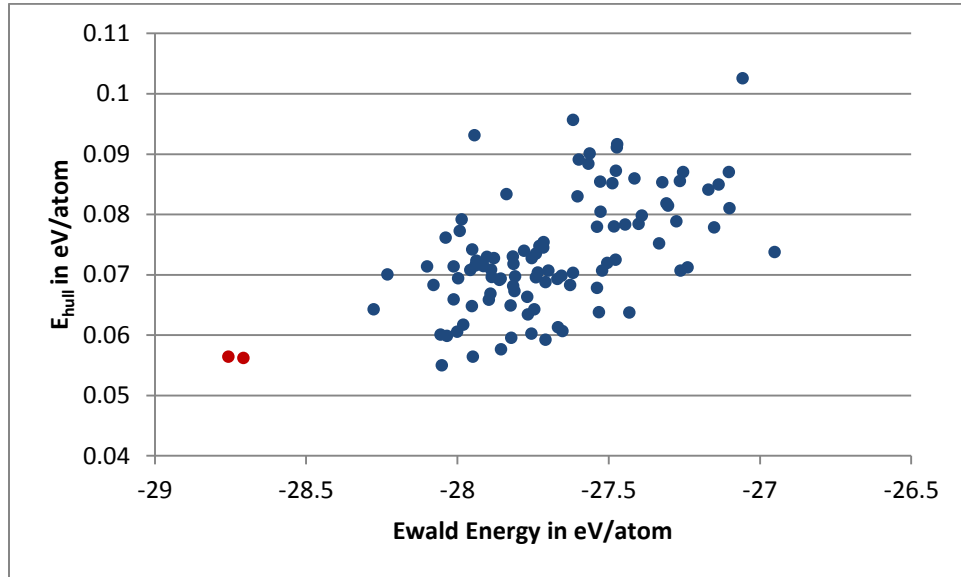


Figure 3.2. Energy above hull (E_{hull} , eV per atom) vs. initial Ewald energy (eV per atom) for 102 undoped δ - Bi_2O_3 structures; includes both random anion orderings (blue) and two ordered states (red) shown in figure 3.1b and c.

The energy of the ordered oxygen sublattice with different configurations were evaluated and compared. For the $\langle 1\ 1\ 1 \rangle$ ordered sublattice in Fig. 3.1.a, the Ewald and E_{hull} values (-26.74 and .205 eV/atom respectively) were high, suggesting this configuration is energetically unfavorable and may not accurately describe the ordered state. For the other $\langle 1\ 1\ 1 \rangle$ ordered configuration in figure 3.1b, the Ewald and E_{hull} energies were -28.76 and 0.0563 eV/atom respectively. Figure 3.1c shows a

$\langle 1\ 1\ 0 \rangle$ ordered configuration. The Ewald and E_{hull} energies were -28.71 and 0.0562 eV/atom respectively. Out of these three ordered states, the $\langle 1\ 1\ 0 \rangle$ ordering shows the lowest energy, and the $\langle 1\ 1\ 1 \rangle$ ordering in figure 3b is comparable.

One of the 100 random configurations generated to evaluate the disordered structure had a lower E_{hull} energy than the $\langle 1\ 1\ 0 \rangle$ configuration. The E_{hull} value was 0.0550 eV/atom and the Ewald energy was -28.38 eV/atom. As can be seen in figure 3.2, the second $\langle 1\ 1\ 1 \rangle$ and $\langle 1\ 1\ 0 \rangle$ structures to have the lowest Ewald energy but other configurations have comparably low E_{hull} values.

Using the method from section 2.5, the predicted order-disorder transition for pure Bi_2O_3 from this study is 207°C. This transition cannot be experimentally observed as the δ phase transitions to the α , β , or γ phases below 650°C. This calculated low transition temperature may be physically reasonable as higher doping concentration tend to order the anion sublattice [12] [8]

Chapter 4 : Effect of Single Dopant Percentage and Ionic Radius

4.1 Lattice Constants

Wachsman *et al.* [13] studied 6 single dopants (Y^{3+} , Yb^{3+} , Ho^{3+} , Er^{3+} , Dy^{3+} , and Tm^{3+}) which were known to stabilize the δ - Bi_2O_3 phase. They demonstrated that the dimensions of the unit cell are proportional to the concentration and ionic radii of the dopant cations (figure 4.1 a). Each of these dopants has a smaller ionic radius than Bi^{3+} . The experimental lattice parameters were proportional to the dopant ionic radius at fixed concentration and inversely proportional to concentration for erbia doped samples.

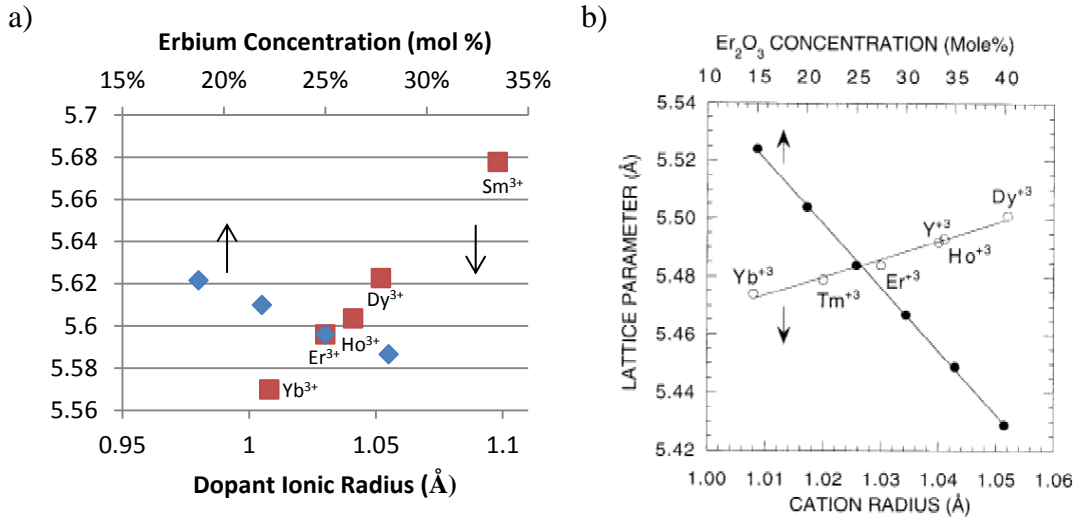


Figure 4.1. Graphs of M^{3+} doped δ - Bi_2O_3 lattice parameter vs M^{3+} ionic radius or Er^{3+} concentration: a) calculated lattice parameters, and b) experimental results by Jiang et al. [13]

We performed first principles DFT calculations to investigate the effects of single dopants on the lattice parameters. All structures were initiated with a unit cell lattice parameter of 5.665 Å (11.33 Å for the 2x2x2 supercell). Five lanthanide dopants (Dy^{3+} , Er^{3+} , Yb^{3+} , Ho^{3+} , and Sm^{3+}) at mol 25% of Bi were evaluated. Samarium (Sm^{3+}) has a larger ionic radius than Dy^{3+} and was beyond what can be done experimentally. Erbium (Er^{3+}) doped Bi_2O_3 , which has the fluorite structure between 15 and 40%, was evaluated at 4 different concentrations (19%, 22%, 25%, and 28%). For each doped composition, 50 initial structures with random cation and anion lattices were evaluated as described in section 2.4. The lowest energy cation configuration was identified. Using the identified lowest energy cation configuration, we re-ordered the oxygen anion sublattice to identify the lowest energy configuration (figure 4.1a). The calculated lattice parameters increase with dopant ionic radius and decrease with dopant concentration. This agrees well with the experimental results, and the predicted lattice parameters are only 2% larger. The trends are linear in agreement with Vegard's law.

4.2 Effect of Er^{3+} concentration on Transition Temperature

We studied the order-disorder transition temperature (T_c) as a function of the Er^{3+} concentration in 19-28% ErSB. Our method calculated a T_c of $\sim 600^\circ\text{C}$ for 19ErSB and $\sim 700^\circ\text{C}$ for 22ErSB, 25ErSB, and 28ErSB (figure 4.2). Experimental results [10] [13] report a value of $\sim 600^\circ\text{C}$ with little change due to concentration. Our results are in reasonable agreement with the experiments. A small increase is observed in energy above hull as doping concentration increases.

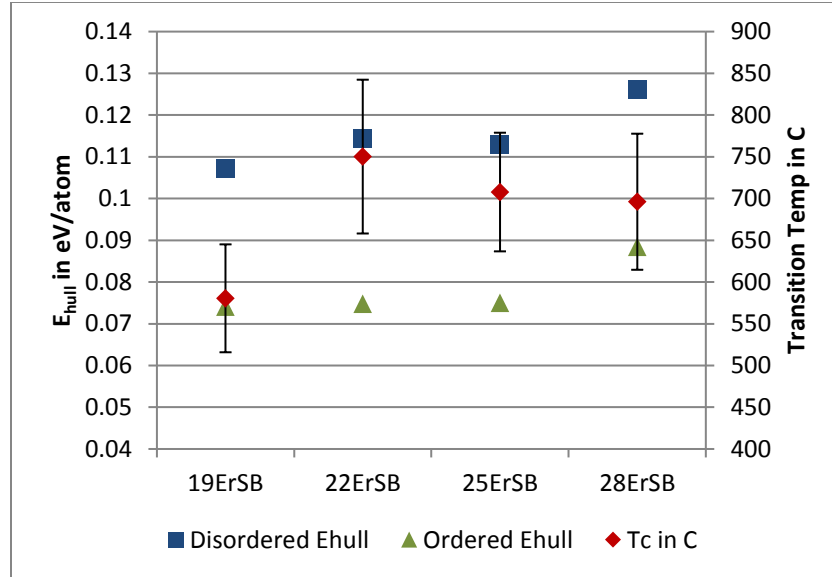


Figure 4.2. Calculated transition temperature (K) and E_{hull} energies (eV/atom) for 19-28% ErSB

4.3 Effect of Single Dopant Type on Transition Temperature

We compared the order-disorder transition for 25% Yb^{3+} , Er^{3+} , Ho^{3+} , Dy^{3+} , and Sm^{3+} doped Bi_2O_3 (figure 4.3). The energy cation configuration was the same for all 25% doped systems. Both the ordered and disordered E_{hull} values decreased as ionic radius decreased. E_{hull} values for 25YbSB do not follow this trend likely because the multivalence nature of Yb. 25DySB and 25SmSB T_c values were $\sim 550^\circ\text{C}$. 25ErSB and 25HoSB T_c values were ~ 700 and 750°C , respectively. Experimental results indicate that transition occurs at $\sim 600^\circ\text{C}$. Our method predicts slightly lower T_c values than experiment, but the relative trend of T_c in change concentration is the key of this study.

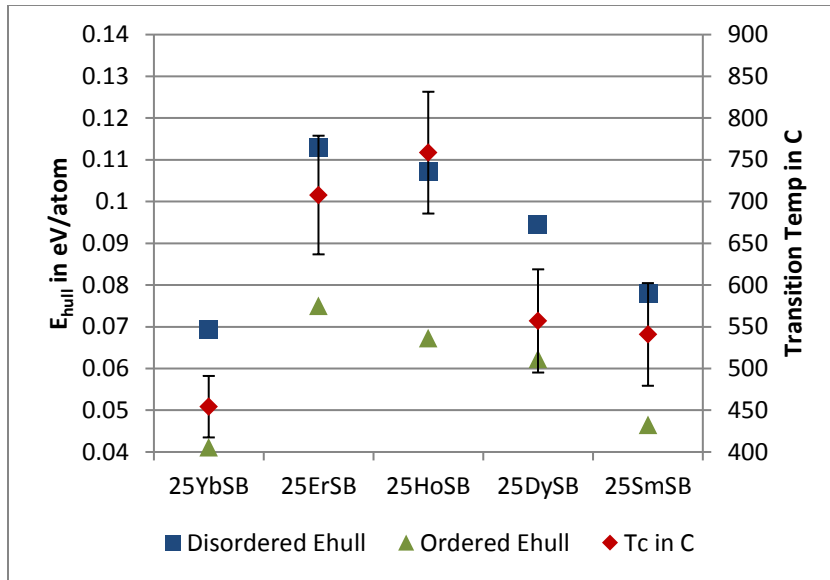


Figure 4.3. Calculated transition temperature (K) and E_{hull} energies (eV/atom) for Yb^{3+} , Er^{3+} , Ho^{3+} , Dy^{3+} , and Sm^{3+} in order of dopant ionic radius

Chapter 5 : Oxygen Sublattice Ordering in Double Doped δ - Bi_2O_3

5.1 Determining Tungsten Dopant Oxidation State

As show in previous experimental studies [34] [16] , the addition of a second dopant increases the entropy of the cation lattice allowing δ - Bi_2O_3 to be stabilized with lower total dopant concentrations. As conductivity increases with decreasing dopant concentration, double doped electrolytes have higher conductivities than single doped electrolytes (Chapter 1). In order to understand fast ionic conduction in double doped DyWSB, one of the highest conductivity electrolytes, we performed DFT calculations to identify the charge and coordination number of the W dopant. While all single cations evaluated in chapter 4 have a 3+ charge, tungsten can exhibit 3+, 4+, 5+, and 6+ oxidations states. The most common oxidation state is 6+ as observed in WO_3 . In order to maintain charge neutrality, cation dopants with higher oxidation states result in higher O^{2-} occupancies, which may significantly impact oxygen sublattice ordering and ionic conductivity.

In our DFT computation, fifty disordered and ordered E_{hull} values were calculated for 12Dy6WSB with 3+, 4+, 5+, and 6+ oxidation states. These values (Fig 5.1) decrease as the oxidation state increases. Therefore, tungsten is expected to remain in the 6+ oxidation state in DyWSB.

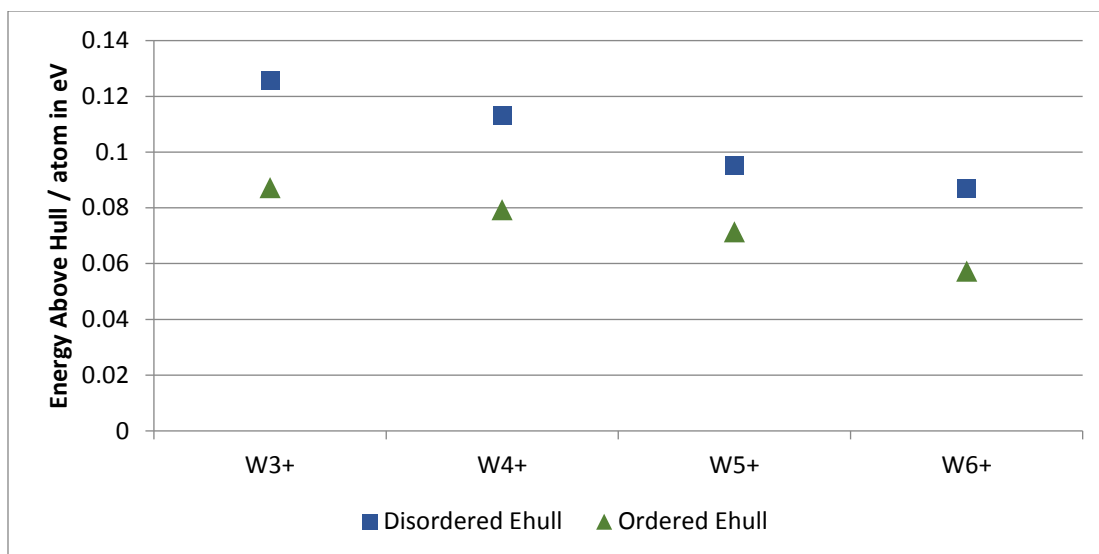


Figure 5.1. Disordered and ordered energy above hull (eV/atom) for 12Dy6WSB for W^{3+} , W^{4+} , W^{5+} , and W^{6+} .

5.2 Determining Oxygen Ordering around Tungsten Dopant

It is not clear whether the W^{6+} dopant, which has a higher charge than Bi^{3+} or Dy^{3+} cations, would order and cluster O^{2-} at adjacent sites. Local ordering around the dopants would negatively impact the ionic conductivity and increase the transition temperature. Since each cation has eight neighboring O^{2-} sites, DFT calculations were performed for 6Dy3WSB with an average of 5, 6, 7, or 8 oxygen ions in the adjacent sites of both W^{6+} dopants. A constant O average occupancy was maintained for the entire supercell.

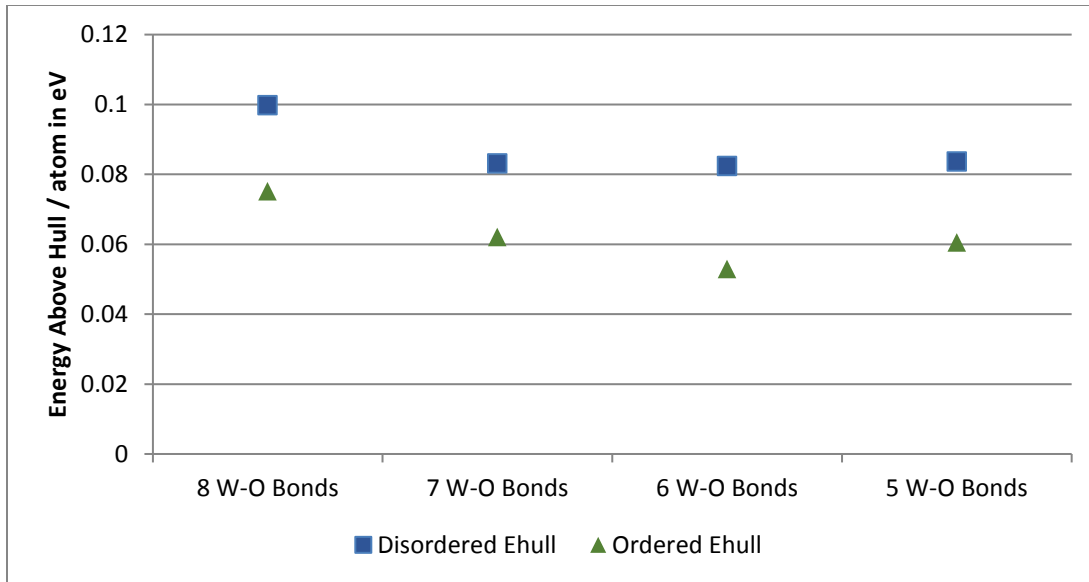


Figure 5.2. Ordered and disordered energy above hull for 6Dy3WSB based on different O^{2-} occupancies at sites neighboring W^{6+} cations

The stability of each configuration was compared (Fig. 5.2). The oxygen sublattice configurations with 8 oxygen ions neighboring each tungsten dopant (8 W-O bonds) have the highest energy in both ordered and disordered states. Therefore, clustering of the extra oxygen around the W^{6+} dopants is the least energetically favorable. Disordered energies were similar for configurations with 5, 6, or 7 W-O bonds, suggesting oxygen ions will occupy both W neighboring and non-W neighboring sites with similar probability in the disordered state. Therefore, the anion sublattice is still disordered after the W doping. The ordered configuration of 6 O around the W^{6+} dopant has the lowest energy. In addition, the local positive charge around the W^{6+} dopant does change the bond lengths around each dopant. In 6Dy3WSB with disordered anion ordering, W-O bonds averaged 2.04 Å compared to 2.34 Å and 2.43 Å for Dy-O and Bi-O bonds respectively. Therefore, W^{6+} dopants do

not order or cluster O^{2-} , and are good dopants for improving oxygen ionic conductivity.

5.3 Calculation of Order-Disorder Transition Temperature

Using the determined tungsten dopant charge and configuration, we calculated T_c and E_{hull} values for both $Dy_2O_3-WO_3$ and $Dy_2O_3-Gd_2O_3$ double doped Bi_2O_3 systems. Concentrations of 6Dy3XSB, 9Dy3XSB, and 12Dy6XSB were compared where X is either the W^{6+} or Gd^{3+} secondary dopant. These concentrations were chosen to be close to the 2:1 dopant ratio and 12 mol% total concentration previously used by experiment [18] and maintain an integer number of ions in each simulation.

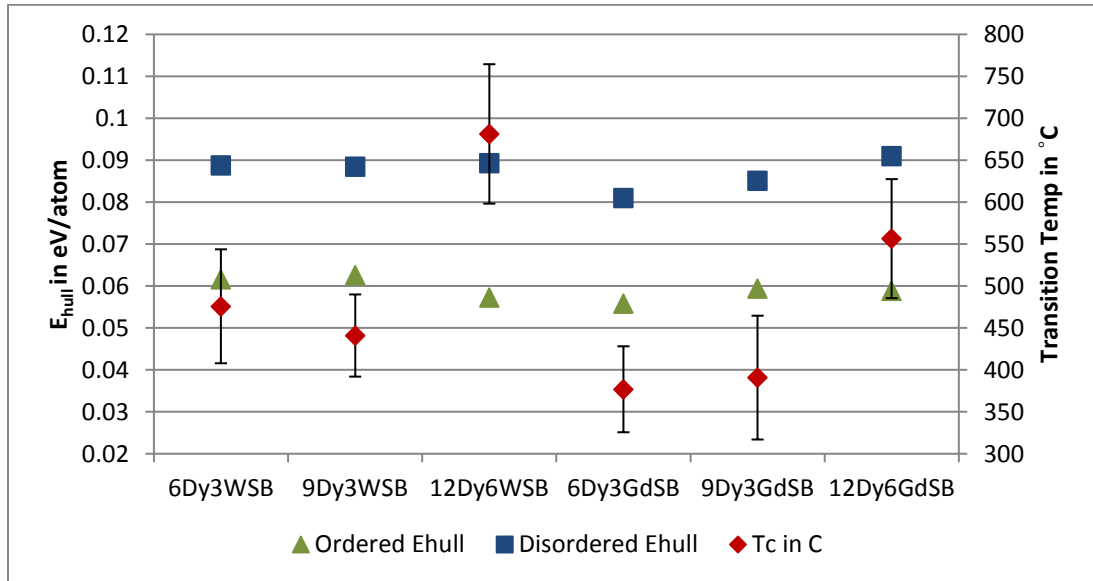


Figure 5.3. Calculated transition temperatures T_c (K) and energies above hull (E_{hull} , eV/atom) for DyW and DyGd doped systems

The T_c values calculated for double doped electrolytes were generally lower than observed for single doped electrolytes (Chapter 4.2-4.3). The T_c value was lowest for 9% and 12% total dopant concentrations. This seems to qualitatively agree

with published Arrhenius plots (Figure 1.3 and 1.4) which demonstrate a curvature in the Arrhenius plot at lower temperatures for double doped cases than 20ErSB. These values are still higher than those calculated for the pure Bi_2O_3 case (Chapter 3.3) as expected if order-disorder transition is influenced by the strength or number of dopant oxygen bonds. The Gd^{3+} doped electrolytes consistently have a lower calculated T_c value than W^{3+} doped equivalents.

Chapter 6 : Computation Prediction of New Dopants

6.1 Prediction of Alternative Double Doping

DFT calculations have been demonstrated to evaluate new doping strategies without the synthesis and characterization of physical materials samples. To identify new alternative Bi_2O_3 electrolyte compositions with lower transition temperatures, we compared combinations of smaller and larger lanthanide dopants in a constant 2:1 ratio and 18 mol% concentration based on 12Dy6GdSB for which Dy^{3+} and Gd^{3+} act as the smaller and larger dopants. Both of these dopants have high polarizability yielding high ionic conductivity. We selected three larger dopants (Gd^{3+} , Sm^{3+} , and Nd^{3+}) and three smaller dopants (Dy^{3+} , Er^{3+} , and Ho^{3+}), which may have large radius to be stabilized in the cubic phase. Each combination was evaluated for E_{hull} and T_c . The same cation and anion configurations as 12Dy6GdSB from section 5.3 were used as the initial structure.

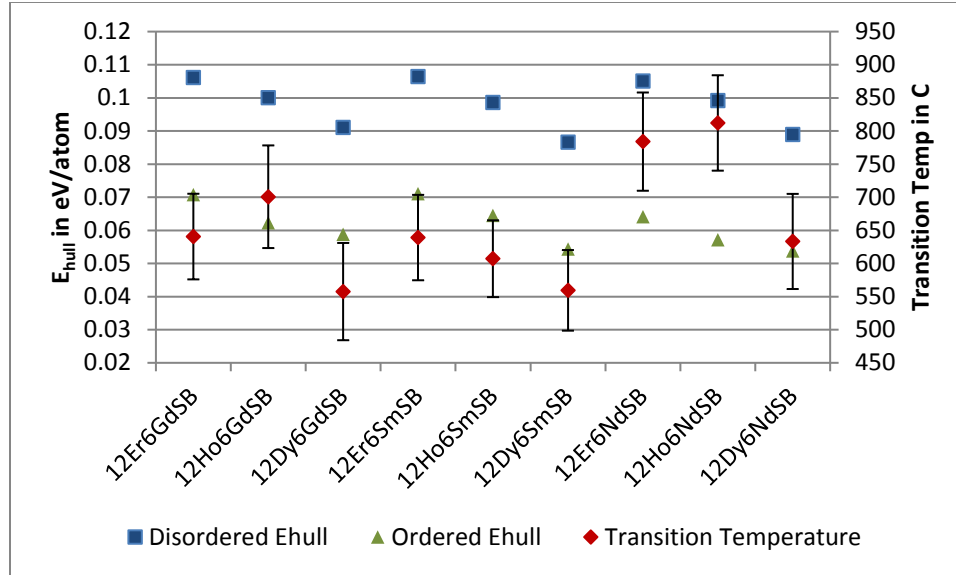


Figure 6.1. Calculated transition temperatures and energies above hull for 9 double doped electrolytes: 12 mol% (Dy, Er, Ho) 6 mol% (Gd, Sm, Nd)

In all cases, the disordered and ordered E_{hull} energies decrease as the radius of the smaller dopant increased. This implies that the smaller dopants indeed stabilized the cubic phases in agreement with previous singled doped samples at 25 mol% (figure 4.3). Calculated transition temperatures for samples doped with Er^{3+} or Ho^{3+} had higher temperatures than the corresponding Dy^{3+} samples. These observations are similar to those observed for 25DySB, 25ErSB, and 25HoSB in section 4.3. Sm^{3+} doped Bi_2O_3 electrolytes have comparable transition temperatures to those doped with Gd^{3+} . Nd^{3+} , which has a larger ionic radius, resulted in higher transition temperatures than the comparable Gd^{3+} and Sm^{3+} cases.

6.2 Prediction of New Dopant for Double Doping

The second method to identify potential alternative dopants used a probabilistic model developed by Ceder et al. [35] [36] and implemented in Pymatgen's "Structure Predictor" module [29]. Using this algorithm, 9 candidate 6+ dopants to substitute W^{6+} in 12Dy6WSB (figure 6.3) and 42 candidate 3+ dopants to substitute Bi^{3+} in 12Dy6GdSB were identified (figure 6.2). A single low energy cation and anion configuration was selected for both Gd^{3+} and W^{6+} cases, and the E_{hull} of those doubled doped compositions was calculated to provide a quick screening of stability (figure 6.2 – 6.3).

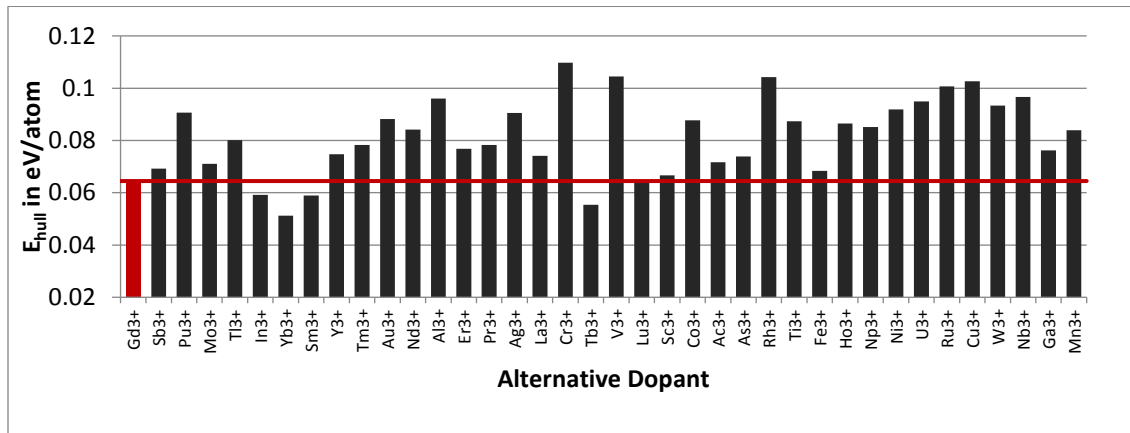


Figure 6.2. E_{hull} energy from single calculation screening experiment for alternatives dopants to Gd^{3+} in 12Dy6GdSB ordered left to right in order of substitution potential for Bi^{3+} cations. Red line indicates E_{hull} for 12Dy6GdSB control.

Of the 42 Gd^{3+} alternatives dopants considered, 18 were selected for further evaluation. The dopants that yield low E_{hull} have more potential to produce stabilized double-doping cubic phase. Therefore, we only selected those with an $E_{hull} < 0.08$ eV/atom for further analysis.

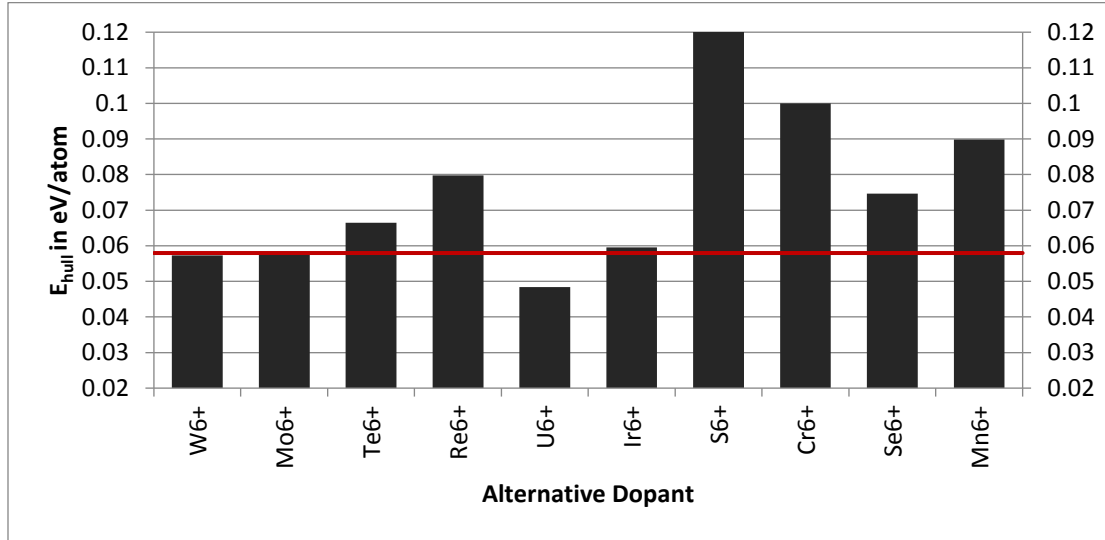


Figure 6.3. E_{hull} energy from single calculation screening experiment for alternatives dopants to W⁶⁺ in 12Dy6WSB ordered left to right in order of substitution potential for W⁶⁺ cations. Red line indicates E_{hull} for 12Dy6WSB control.

Of the 9 W⁶⁺ alternatives dopants considered Mn⁶⁺, Cr⁶⁺, S⁶⁺, and Re⁶⁺ were excluded as the energy above hull exceeded 0.08 eV/atom. The remaining 5 were evaluated further as they are more likely to produce a stable cubic double doped system.

A three-step method was used to screen potential dopants that provide both decent stability and lower T_c values.

- E_{hull} for each alternative dopant was calculated based on a fixed cation configuration identified in chapter 5 and 50 initial anion configurations. This step was used to calculate E_{hull} more accurately than could be done with the single calculations shown in figures 6.2 and 6.3. Dopants with 6+ oxidation states were evaluated further if E_{hull} values were less than observed for W⁶⁺. Dopants with 3+

oxidations states were evaluated further if the average E_{hull} energy was less than 0.085eV or predicted T_c was less than 400°C.

- In order to confirm that the cation configuration was appropriate for each dopant, 100 disordered cations configurations were evaluated for each remaining dopant. No potential new dopants were eliminated at this stage.
- Finally, E_{hull} and T_c were calculated based on the fixed cation ordering identified during the second step. As this method is more likely to underestimate T_c by failing to find low energy anion orderings that overestimate it, only the fixed cation ordering (first or third step) which predicted the higher transition temperature is reported in figure 6.4.

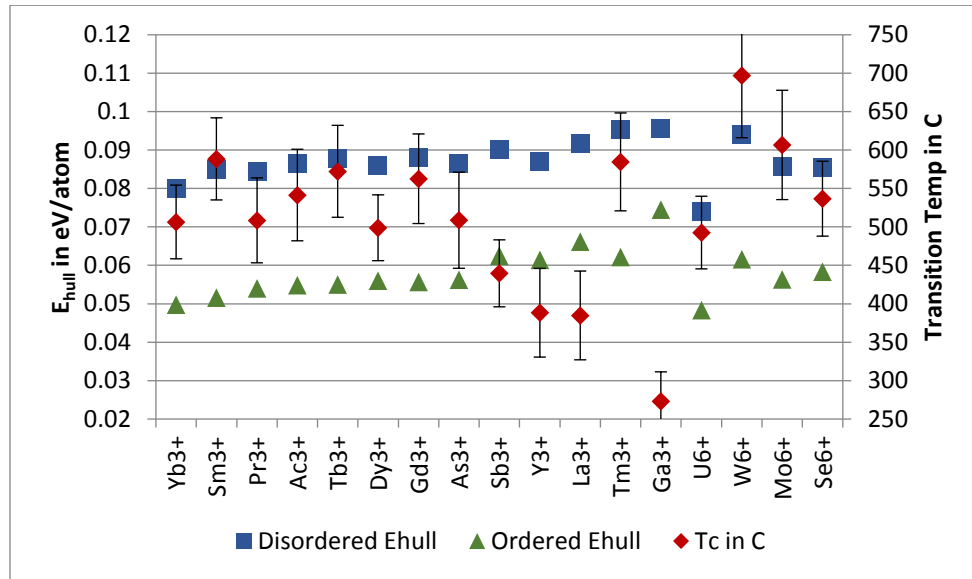


Figure 6.4. Predicted transition temperatures and energies above hull for 12Dy6XSb

(X is the proposed secondary dopant).

This method predicts several potential alternative 3+ dopants with T_c values less than 12Dy6GdSB. Gallium (Ga^{3+}) has the lowest predicted T_c value but is potentially unstable due to the high ordered and disordered E_{hull} values. Lanthanum (La^{3+}), Antimony (Sb^{3+}), and Yttrium (Y^{3+}) doped $\delta\text{-Bi}_2\text{O}_3$ had T_c values around 400-450°C but all three ordered E_{hull} values were higher than Gd^{3+} . These doped structures may be stable as E_{hull} is only .01 eV/atom higher. Other remaining dopants had comparable T_c and E_{hull} values to Gd^{3+} . Yb^{3+} and Sm^{3+} were the most stable according to this analysis. As^{3+} may be toxic and Ac^{3+} is radioactive. Pr^{3+} however might make the electrolyte electrically conductive as it has multiple low energy oxidation states.

U^{6+} , Mo^{6+} , and Se^{6+} had lower calculated E_{hull} and T_c values than W^{6+} . Of these U^{6+} is predicted to be the most stable and have the lowest T_c but is likely impractical for most applications as it is radioactive. Mo^{6+} has a common 4+ oxidation state and is, therefore, likely to induce electronic conductivity.

Several of these alternative dopants from our computation have been previously considered in literature. Meng et al. determined that Y^{3+} , Mo^{6+} , and W^{6+} help stabilize the cubic phase and La^{3+} , $\text{Pr}^{3+/4+}$, Sm^{3+} , and Gd^{3+} help stabilize the rhombohedral phase [34]. Jung et al. successfully produced Terbium (Tb^{3+}) and Tungsten co-doped Bi_2O_3 as a potential electrolyte and reported a T_c between 500°C and 600°C [37]. Lazzaraga et al. produced 12La12USB (6% La_2O_3 , 12% UO_3 , 88% Bi_2O_3) but reported a bend in the Arrhenius plot at 550°C [38]. This shows that these dopants can be used in co-doped $\delta\text{-Bi}_2\text{O}_3$ electrolytes. While these reports often do not note changes in the T_c value, this is likely due to the difficulty in accurately measuring this for a small number of samples. The order-disorder transition for

double doped electrolytes is observed as a curved line in the Arrhenius plots as opposed the sharp bend in single doped systems. Additional experimental measurements are likely needed to accurately calculate and compare the order-disorder transition temperature.

Chapter 7 : Future Work and Conclusions

7.1 Computation Error

The error bars associated with the T_c calculations are quite large. They also rely on finding the lowest energy anion ordering via random sampling which can be unreliable. Increasing the number of configurations for each T_c value, increasing the number of k points, or decreasing energy cutoffs are likely to reduce the standard error though increase computing time. A computation method to identified the lowest energy ordered structure would be highly desired.

7.2 Additional Alternative Dopants

This study aims to discover useful alternative doping strategies. However, it is possible that several dopants that may have potential were neglected. Of 49 alternative dopants which were identified by Pymatgen's "Structure Predictor", only 23 were evaluated beyond the initial screening. This was based on an energy cutoff from a single initial configuration. As in 25DySB compared to 25YbSB, the value of E_{hull} could be higher due to different preferential cation orderings. Some dopants may have been eliminated prematurely.

All alternative dopants considered had either a 3+ or 6+ charge as they could be readily compared to DyGdSB and DyWSB. Meng et al. observed that Nb₂O₅ could stabilize the cubic phase while BaO and SrO could stabilize the rhombohedral

phase. These dopants were not considered in this thesis. A new study may consider dopants with 5+ and 2+ charges.

Finally, most double doping calculations still used Dy^{3+} as the primary dopant while varying the secondary dopant. Additional calculations with alternative primary dopants may discover other low T_c materials.

7.3 Estimating phase stability

We use E_{hull} as a reasonable estimate for the overall stability of doped materials. However, it does not consider other phases of Bi_2O_3 and alternative crystal structures not available in Materials Project. Alternative phases such as the rhombohedral phase may be more stable at the predicted transition temperatures as described in sections 1.3 and 1.4. In addition, DFT calculations are at 0K, which may not reflect the change in other terms in the free energy.

7.4 Experimental Verification

Experimental synthesis and measurements is required to test and verify the predicted new doping. These experiments also need to confirm whether the dopants have a detrimental effect on ionic conductivity or electrical insulation.

7.5 Conclusion

This thesis presents a first principles computation study to predict new dopants for stabilized $\delta\text{-Bi}_2\text{O}_3$ electrolytes. We determined the tungsten cation charge and anion ordering behavior in DyWSB electrolytes and predicted various alternative secondary dopants. Several of the predicted dopants are supported by literature results. The effects of dopant radius and concentration on the stability and transition

temperature are studied for both single-doping and double-doping systems. Multiple new dopants are predicted for stabilizing the δ -Bi₂O₃ materials and decreasing the transition temperature. This study provides significant insights for future research and development on oxygen ionic conductor materials.

Bibliography

- [1] E. D. Wachsman and K. T. Lee, "Lowering the Temperature of Solid Oxide Fuel Cells," *Science*, vol. 334, no. 6058, pp. 935-939, 2011.
- [2] J. A. Kilner and M. Burriel, "Materials for Intermediate-Temperature Solid-Oxide Fuel Cells," *Annu. Rev. Mater. Res. Annual Review of Materials Research*, pp. 365-93, 2014.
- [3] K. T. Lee, H. S. Yoon and E. D. Wachsman, "The Evolution of Low Temperature Solid Oxide Fuel Cells," *Journal of Materials Research*, vol. 27, no. 16, pp. 2063-2078, 2012.
- [4] "HYDROGEN PRODUCTION PROCESSES," US Department of Energy, Office of Energy Efficiency & Renewable Energy, [Online]. Available: <http://energy.gov/eere/fuelcells/hydrogen-production-processes>. [Accessed 3 2016].
- [5] B. Dunn, H. Kamath and J.-M. Tarascon, "Electrical Energy Storage for the Grid: A Battery of Choices," *Science*, vol. 334, no. 6058, pp. 928-935, 2011.
- [6] D. S. Aidhy, S. B. Sinnott, E. D. Wachsman, S. R. Phillpot and J. C. Nino, "Structure of δ -Bi₂O₃ from Density Functional Theory: A Systematic Crystallographic Analysis," *Journal of Solid State Chemistry*, vol. 182, no. 5, pp. 1222-1228, 2009.
- [7] G. Gattow and H. Schroder, "Uber Wismutoxide. III. Die Kristallstruktur der Hochtemperaturmodifikation von Wismuth(III)-oxid (δ -Bi₂O₃)," *Zeitschrift fur anorganische und allgemeine Chemie*, vol. 318, no. 3-4, pp. 176-189, 1962.
- [8] G. Malmros, "The Crystal Structure of α -Bi₂O₃," *Acta Chemica Scandinavica*, vol. 24, pp. 384-396, 1970.
- [9] M. J. Verkerk and A. J. Burggraaf, "HIGH OXYGEN ION CONDUCTION IN SINTERED OXIDES OF THE BISMUTH OXIDE-DYSPROSIUM OXIDE (Bi₂O₃-Dy₂O₃) SYSTEM," *Chemischer Informationsdienst*, vol. 12, no. 17, pp. 75-82, 1981.
- [10] M. J. Verkerk, K. Keizer and A. J. Burggraaf, "High Oxygen Ion Conduction in Sintered Oxides of the Bi₂O₃-Er₂O₃ System," *J Appl Electrochem Journal of Applied Electrochemistry*, vol. 10, no. 1, pp. 81-90, 1980.
- [11] T. Takahashi, T. Esaka and H. Iwahara, "High Oxide Ion Conduction in the Sintered Oxides of the System Bi₂O₃-Gd₂O₃," *Journal of Applied Electrochemistry*, vol. 5, no. 3, pp. 197-202, 1975.
- [12] N. M. Sammes, G. A. Tompsett, H. Näfe and F. Aldinger, "Bismuth Based Oxide Electrolytes— Structure and Ionic Conductivity," *Journal of the European Ceramic Society*, vol. 19, no. 10, pp. 1801-1826, 1999.
- [13] N. Jiang and E. Wachsman, "Structural stability and conductivity of phase stabilized cubic bismuth oxides," *Journal of the American Ceramic Society*, vol. 82, no. 11, pp. 3057-3064, 1999.

- [14] S. Boyapati, E. Wachsman and B. Chakoumakos, "Neutron diffraction study of occupancy and positional order of oxygen ions in phase stabilized cubic bismuth oxides," *Solid State Ionics*, vol. 138, no. 3-4, pp. 293-304, 2001.
- [15] P. Battle, C. Catlow, J. Heap and L. Moroney, "Structural and Dynamical Studies of delta-Bi₂O₃ Oxide Ion Conductors I. The Structure of (Bi₂O₃)_{1-x}(Y₂O₃)_x as a Function of x and Temperature," *Journal of Solid State Chemistry*, vol. 63, no. 1, pp. 8-15, 1986.
- [16] N. Jiang, E. Wachsman and S. Jung, "A higher conductivity Bi₂O₃-based electrolyte," *Solid State Ionics*, vol. 150, no. 1, pp. 347-353, 2002.
- [17] D. W. Jung, K. L. Duncan, M. A. Camaratta, K. T. Lee, J. C. Nino and E. D. Wachsman, "Effect of Annealing Temperature and Dopant Concentration on the Conductivity Behavior in (DyO_{1.5})_x-(WO₃)_y-(BiO_{1.5})_{1-x-y}," *Journal of the American Ceramic Society*, vol. 93, no. 5, pp. 1384-1391, 2010.
- [18] D. Jung, K. Duncan and E. Wachsman, "Effect of total dopant concentration and dopant ratio on conductivity of (DyO_{1.5})_x-(WO₃)_y-(BiO_{1.5})_(1-x-y)," *Acta Materialia*, vol. 58, no. 2, pp. 355-363, 2010.
- [19] D. W. Jung, K. T. Lee and E. D. Wachman, "Dysprosium and Gadolinium Double Doped Bismuth Oxide Electrolytes for Low Temperature Solid Oxide Fuel Cells," *Journal of the Electrochemical Society*, vol. 163, no. 5, pp. F411-415, 2016.
- [20] G. Kresse and J. Hafner, "Ab initio molecular dynamics for liquid metals," *Phys. Rev. B*, vol. 47, p. 558, 1993.
- [21] G. Kresse and J. Hafner, "Ab initio molecular-dynamics simulation of liquid metal amorphous semiconductor transition in germanium," *Phys. Rev. B*, vol. 49, p. 14251, 1994.
- [22] G. Kresse and J. Furthmuller, "Efficiency of ab-initio total energy calculations for metals and semiconductors using a plane wave basis set," *Computational Material Science*, vol. 6, p. 15, 1996.
- [23] G. Kresse and J. Furthmuller, "Efficient iterative schemes for ab initio total-energy calculations using a plane wave basis set," *Phys. Rev. B*, vol. 54, p. 11169, 1996.
- [24] P. E. Blochl, "Projector augmented-wave method," *Phys. Rev. B*, vol. 50, p. 17953, 1994.
- [25] G. Kresse and D. Joubert, "From ultrasoft pseudopotentials to the projector augmented wave method," *Phys. Rev. B*, vol. 59, p. 1758, 1999.
- [26] J. Perdew, K. Burke and M. Ernzerhof, "Erratum: Generalized gradient approximation made simple," *Phys. Rev. Lett.*, vol. 78, p. 1396, 1997.
- [27] J. Perdew, K. Burke and M. Ernzerhof, "Generalized gradient approximation made simple," *Phys. Rev. Lett.*, vol. 77, p. 3865, 1996.
- [28] S. P. Ong, W. D. Richards, A. Jain, G. Hautier, M. Kocher, S. Cholia, D. Gunter, V. Chevrier, K. A. Persson and G. Ceder, "Python Materials Genomics (pymatgen) : A Robust, Open-Source Python Library for Materials Analysis," *Computational Materials Science*, vol. 68, pp. 314-319, 2013.

- [29] A. Jain, S. Ong, G. Hautier, W. Chen, W. Richards, S. Dacek, S. Cholia, D. Gunter, D. Skinner, G. Ceder and K. Persson, "The Materials Project: A materials genome approach to accelerating materials innovation," *APL Materials*, vol. 1, no. 1, 2013.
- [30] A. Jain, G. Hautier, S. Ong, C. Moore, C. Fischer, K. Persson and G. Ceder, "Formation enthalpies by mixing GGA and GGA+U calculations," *Physical Review B*, vol. 84, no. 4, 2011.
- [31] S. Ong, L. Wang, B. Kang and G. Ceder, "Li-Fe-P-O₂ Phase Diagram from First Principles Calculations," *Chemistry of Materials*, vol. 20, no. 5, pp. 1798-1807, 2008.
- [32] L. Sillen, "XRay Studies on Bismuth Trioxide," *Arkiv foer Kemi Mineralogi och Geologi*, vol. 12, no. 18, pp. 1-15, 1938.
- [33] E. Wachsman, S. Boyapati, M. Kaufman and N. Jiang, "Modeling of Ordering Structures of Phase Stabilized Cubic Bismuth Oxides," *Journal of American Ceramic Society*, vol. 83, no. 8, pp. 1964-1968, 2000.
- [34] G. Meng, C. Chen, X. Han, P. Yang and D. Pend, "Conductivity of Bi₂O₃-Based Oxide Ion Conductors with Double Stabilizers," *Solid State Ionics*, vol. 28, no. 1, pp. 533-538, 1988.
- [35] G. Hautier, C. Fischer, V. Ehrlacher, A. Jain and G. Ceder, "Data Mined Ionic Substitutions for the Discovery of New Compounds," *Inorganic Chemistry*, vol. 50, no. 2, pp. 656-663, 2011.
- [36] A. Jain, G. Hautier, C. Moore, S. Ong, C. Fischer, T. Mueller, K. Persson and G. Ceder, "A high-throughput infrastructure for density functional theory calculations," *Computational Materials Science*, vol. 50, pp. 2295-2310, 2011.
- [37] D. W. Jung, K. T. Lee and E. D. Wachsman, "Terbium and Tungsten Co-doped Bismuth Oxide Electrolytes for Lower Temperature Solid Oxide Fuel Cells," *Journal of the Korean Ceramic Society*, vol. 51, no. 4, pp. 260-264, 2014.
- [38] M. Lazarraga, F. Pico, J. Amarilla, R. Rojas and J. Rojo, "The cubic Bi_{1.76}U_{0.12}La_{0.12}O_{3.18} mixed oxide: Synthesis, structural characterization, thermal stability, and electrical properties," *Solid State Ionics*, vol. 126, no. 1, pp. 2313-2318, 2005.
- [39] A. Tarancon, "Strategies for Lowering Solid Oxide Fuel Cell Operating Temperature," *ENERGIES*, vol. 2, no. 4, pp. 1130-1150, 2009.
- [40] K. Momma and F. Izumi, "VESTA 3 for three dimensional visualization of crystal, volumetric, and morphology data," *Journal of Applied Crystallography*, vol. 44, pp. 1272-1276, 2011.
- [41] K. Momma and F. Izumi, "VESTA: a three-dimensional visualization system for electronic and structural analysis," *Journal of Applied Crystallography*, vol. 41, pp. 653-658, 2008.